

THE HUBBLE DEEP FIELD SOUTH: FORMULATION OF THE OBSERVING CAMPAIGN

ROBERT E. WILLIAMS,¹ STEFI BAUM,¹ LOUIS E. BERGERON,¹ NICHOLAS BERNSTEIN,¹ BRETT S. BLACKER,¹ BRIAN J. BOYLE,²
THOMAS M. BROWN,^{3,4} C. MARCELLA CAROLLO,^{5,6,7} STEFANO CASERTANO,¹ RICCARDO COVARRUBIAS,⁸
DUÍLIA F. DE MELLO,¹ MARK E. DICKINSON,¹ BRIAN R. ESPEY,¹ HENRY C. FERGUSON,¹
ANDREW FRUCHTER,¹ JONATHAN P. GARDNER,³ ANNE GONNELLA,¹ JEFFREY HAYES,¹
PAUL C. HEWETT,⁹ INGER HEYER,¹ RICHARD HOOK,¹⁰ MIKE IRWIN,⁹ DANIEL JONES,¹
MARY ELIZABETH KAISER,³ ZOLT LEVAY,¹ ANDY LUBENOW,¹ RAY A. LUCAS,¹
JENNIFER MACK,¹ JOHN W. MACKENTY,¹ PIERO MADAU,¹ RUSSELL B. MAKIDON,¹
CRYSTAL L. MARTIN,^{1,6} LISA MAZZUCA,¹ MAX MUTCHLER,¹ RAY P. NORRIS,¹¹
BETH PERRIELLO,¹ M. M. PHILLIPS,⁸ MARC POSTMAN,¹ PATRICIA ROYLE,¹
KAILASH SAHU,¹ SANDRA SAVAGLIO,¹ ALISON SHERWIN,¹ T. ED SMITH,¹
MASSIMO STIAVELLI,¹ NICHOLAS B. SUNTZEFF,⁸ HARRY I. TEPLITZ,^{3,4}
ROELAND P. VAN DER MAREL,¹ ALISTAIR R. WALKER,⁸
RAY J. WEYMANN,¹² MICHAEL S. WIGGS,¹
GERARD M. WILLIGER,^{3,4} JENNIFER WILSON,¹
NORBERT ZACHARIAS,^{8,13} AND DAVID R. ZUREK¹

Received 2000 June 2; accepted 2000 August 23

ABSTRACT

Deep, multiband observations of high Galactic latitude fields are an essential tool for studying topics ranging from Galactic structure to extragalactic background radiation. The Hubble Deep Field (HDF-N) observations obtained in 1995 December established a standard for such narrow, deep surveys. The field has been extensively analyzed by a variety of groups and has been widely studied with imaging and spectroscopy over wavelengths ranging from 10^{-3} to $2 \times 10^5 \mu\text{m}$. We describe here a second deep field campaign (HDF-S), this time in the southern hemisphere, undertaken by the *Hubble Space Telescope* (*HST*) in 1998 October in a program very similar to the northern Hubble Deep Field. Imaging and spectroscopy of three adjacent fields in the southern continuous viewing zone were obtained simultaneously for 150 orbits, and a mosaic of flanking fields was imaged for 27 additional orbits. Two important features of the HDF-S distinguish it from the HDF-N: the campaign included parallel observations by the three main *HST* instruments—WFPC2, STIS, and NICMOS—and the HDF-S location was selected to place a bright $z = 2.24$ quasar in the STIS field of view. The HDF-S observations consist of WFPC2 images in filters close to U , B , V , and I , a deep STIS image of the field surrounding the quasar, spectroscopy of the quasar with STIS from 1150 to 3560 Å, and deep imaging of an adjacent field with NICMOS camera 3 at 1.1, 1.6, and 2.2 μm . All of the HDF-S data were fully reduced and made publicly available within 2 months of the observations, and we describe here the selection of the fields and the observing strategy that was employed. Detailed descriptions of the data and the reduction techniques for each field, together with the corresponding source catalogs, appear in separate papers.

Key words: catalogs — cosmology: observations — galaxies: evolution — galaxies: formation — galaxies: photometry — surveys

1. INTRODUCTION

The original Hubble Deep Field (HDF-N) was undertaken in 1995 December with the aim of creating an observing program that could provide a common focus for a variety of studies requiring a deep, high-resolution optical

image at high Galactic latitude (Williams et al. 1996). A field was selected in the northern “continuous viewing zone,” and 150 orbits of *Hubble Space Telescope* (*HST*) Director’s Discretionary Time were devoted to the observations. The observations represented a significant advance in depth and

¹ Space Telescope Science Institute, 3700 San Martin Drive, Baltimore, MD 21218.

² Anglo-Australian Observatory, P.O. Box 296, Epping, NSW 2121, Australia.

³ Laboratory for Astronomy and Solar Physics, Code 681, Goddard Space Flight Center, Greenbelt, MD 20771.

⁴ NOAO Research Associate.

⁵ Department of Physics and Astronomy, Johns Hopkins University, 3400 North Charles Street, Baltimore, MD 21218-2686.

⁶ Hubble Fellow.

⁷ Current address: Department of Astronomy, Mail Code 5246, Columbia University, 550 West 120th Street, New York, NY 10027.

⁸ Cerro Tololo Inter-American Observatory, Casilla 603, La Serena, Chile.

⁹ Institute of Astronomy, University of Cambridge, Madingley Road, Cambridge CB3 0HA, UK.

¹⁰ Space Telescope European Coordinating Facility, Karl-Schwarzschild-Strasse 2, D-85748 Garching, Germany.

¹¹ Australia Telescope National Facility, P.O. Box 76, Epping, NSW 2121, Australia.

¹² Observatories of the Carnegie Institution of Washington, 813 Santa Barbara Street, Pasadena, CA 91109.

¹³ US Naval Observatory, 3450 Massachusetts Avenue, NW, Washington, DC 20392-5420.

wavelength information over previous *HST* observations. The data were reduced rapidly and widely distributed to stimulate follow-up observations and study.

The HDF-N campaign was successful in creating a unique data set that was central to a number of topics in galaxy evolution. It also served as the impetus to push the performance capabilities of the Wide Field Planetary Camera 2 (WFPC2) and to develop observing procedures to remove detector signatures and to recover subpixel spatial resolution. These developments have found application to many subsequent *HST* observations, e.g., the dithering and the “drizzling” techniques that were developed for the HDF-N (Fruchter & Hook 1998).

The effectiveness of the HDF-N data was aided immeasurably by ground-based follow-up observations of the galaxies in the field that produced spectroscopic redshifts by the various consortia using the 10 m Keck Telescopes (Cohen et al. 1996; Hogg et al. 1998; Lowenthal et al. 1997). These confirmed the utility of selecting *U*- and *B*-band “dropouts” (Steidel et al. 1996; Madau et al. 1996) as criteria for identifying high-redshift objects, and the validity of photometric redshifts derived from broadband data (Gwyn & Hartwick 1996; Lanzetta, Yahil, & Fernández-Soto 1996; Mobasher et al. 1996; Connolly et al. 1997; Sawicki, Lin, & Yee 1997). The latter technique provides approximate distances for even the faintest objects that can be imaged, thereby opening them to cosmological interpretation.

Because of the wealth of data from *HST* and the Keck redshift studies, the HDF-N was a natural target for studies at other wavelengths. The connection between distant galaxies and microjansky radio sources was studied through deep VLA and MERLIN observations (Fomalont et al. 1997; Richards et al. 1998; Muxlow et al. 1999). Wilner & Wright (1997) used 2.8 mm observations of the HDF-N to set limits on the number of luminous dusty star-forming galaxies at high redshift, while others (Rowan-Robinson et al. 1997; Hughes et al. 1998; Aussel et al. 1999; Désert et al. 1999) detected possible examples of such objects using the *Infrared Space Observatory* and the SCUBA submillimeter bolometer array on the James Clerk Maxwell Telescope. Follow-up observations in the near-IR were carried out from KPNO and Keck (Hogg et al. 1997; Dickinson 1998) and from *HST* (Thompson et al. 1999; Dickinson et al. 2000), as were optical and UV observations from *HST* (Gilliland, Nugent, & Phillips 1999; Ferguson et al. 2000a).

The impact of the northern field and the fact that *HST* had acquired new capabilities from two additional instruments—the Space Telescope Imaging Spectrograph (STIS) and Near Infrared Camera and Multi-Object Spectrometer (NICMOS), installed during the second servicing mission, in 1997—made the possibility of a second HDF campaign very attractive. At the time of the HDF-N observations, consideration had been given to locating the field around a distant quasar in order to provide for a line of sight against which to detect intervening gas via Ly α absorption. This would have added an interesting dimension to the HDF-N imaging data set; however, the idea was not implemented, both because of concern that galaxies associated with the quasar might skew the galaxy number counts, which were anticipated to be one of the key results that would come out of the HDF-N observations, and also because of the fact that the positions of candidate quasars known to be situated within the northern continuous

viewing zone (CVZ) did not provide for good CVZ passages. As a result, a random, nondescript field was finally selected for the HDF-N.

The idea of choosing a line of sight that includes a relatively bright QSO was revived for the Hubble Deep Field South (HDF-S) campaign. In this case, the possibility that the galaxy number counts might be skewed by the QSO was viewed as only a minor issue, because the HDF-N had already established the reference faint-galaxy counts in a non-QSO field. Furthermore, the excess in number counts introduced by companions to the QSO would likely amount to only a handful of galaxies, even if the QSO were located in a rich cluster. Thus, the bias introduced by the QSO is not a serious problem for the use of the field for general surveys, and it is offset by the value of having intervening absorption systems to provide a probe of gas along the line of sight. The large amount of *HST* and ground-based observing already devoted to searching for galaxies associated with QSO absorbers indicates a strong interest in such studies, and the location of a QSO in the HDF-S field offers the opportunity to obtain the deep images and, to some extent, follow-up spectroscopy more or less “for free” since these measurements will be made for the field galaxy surveys anyway.

The HDF campaigns help maximize the value returned from deep surveys. The location in the CVZ is selected to maximize the efficiency of *HST*, which is the most expensive instrument being used for such surveys. The availability of *HST* provides a strong motivation for other facilities to invest a significant fraction of their “deep survey” time observing the same field, and the availability of such a wide variety of information on the same patch of sky motivates extensive modeling efforts. Viewed in this light, the southern CVZ was clearly a logical place for the next *HST* deep survey. The advent of 8 m class telescopes in the Southern Hemisphere made it clear that high-resolution images of a southern deep field would eventually be desirable, and it seemed sensible to choose a field that would again maximize *HST* observing efficiency. The decision was thus made to devote a large fraction of Cycle 7 Director’s Discretionary Time to a southern HDF campaign, similar in character to the HDF-N campaign, but with the added benefit of a QSO in the field and parallel observations by the new instruments.

2. FIELD SELECTION

HST continuous viewing zones occur at the poles of the telescope’s orbit, i.e., at declinations of $\pm 62^\circ$, and they have an approximate size of some 5° depending upon the length of the continuous observing that is desired. The precession of the telescope’s orbit causes the CVZs to sweep in circles around the celestial poles every 8 weeks. For a small range of declinations, the CVZs can offer continuous observing for periods of up to 8 days uninterrupted by Earth occultation (but punctuated on roughly half the orbits by passages through the South Atlantic Anomaly).

The major drawback of such an observing geometry is that the line of sight is always close to Earth’s limb. Scattered earthshine is therefore a factor during the daylight half of the orbit, resulting in a higher background for CVZ observations than normally encountered along lines of sight in other directions. This can be a limitation for observations involving the detection of faint sources. One way to counteract the higher background is to devote bright-time

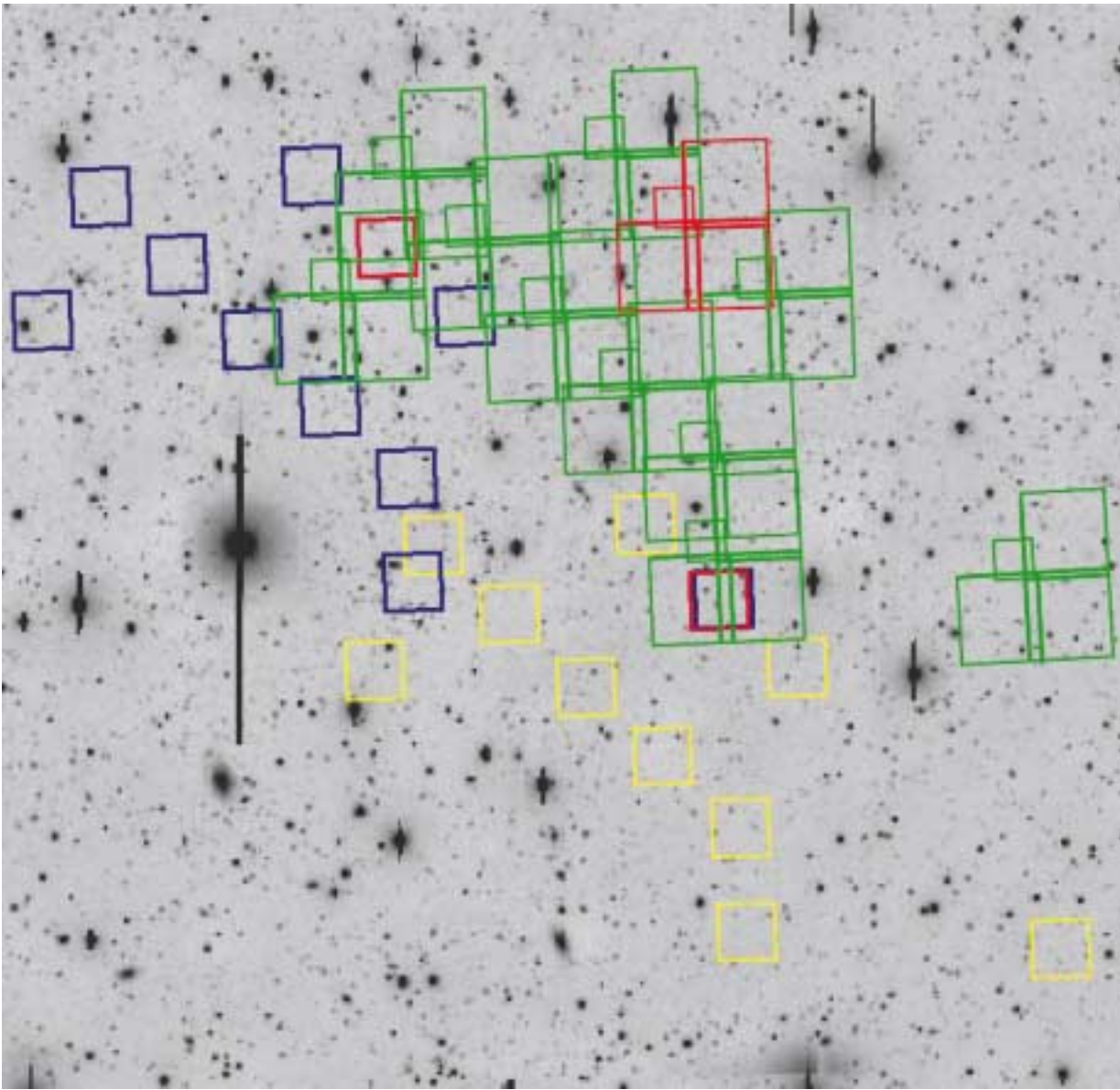


FIG. 1.—Footprints of the three *HST* instruments WFPC2, STIS, and NIC3 as oriented for the HDF-S observations, superposed on a CTIO 4 m image of the region. The 150-orbit primary fields are outlined in red, with the $50'' \times 50''$ STIS field to the upper left (northeast) having the quasar centered in it. The nine contiguous two-orbit WFPC2 flanking fields surrounding the primary WFPC2 field are shown in green, and the corresponding images from STIS and NIC3 that were taken in parallel are shown in blue and yellow, respectively. The NIC3 primary field was observed with STIS for nine orbits to provide optical imagery. Thus the blue outline on the NICMOS primary field represents the deeper STIS optical image, and the offset green outline of the WFPC2 field at the western edge shows the area covered by the nine-orbit F606W + F814W parallel WFPC2 image taken at the same time. There is a bright ($V = 7$) star 7' to the north of the primary WFPC2 field.

observations to spectroscopy or to imaging in bandpasses where low throughput causes noise from sources other than the scattered background, e.g., read noise or the telescope's own radiation in the IR, to be the limiting factors. In such a situation the CVZ offers double the observing time normally available per orbit, so we undertook to identify candidate areas of the sky within the southern CVZ with low extinction and N_{HI} , and devoid of strong radio sources, as potential HDF-S fields. Unfortunately, no known quasars were found to exist within any of these candidate regions, and therefore we initiated several programs to identify quasars within suitable areas of the southern CVZ.

Fortunately, UK Schmidt Telescope objective-prism plates of some of the candidate fields were found to exist,

and these were scanned by the Automatic Plate Measuring (APM) machine at the Institute of Astronomy, Cambridge, and searched for quasars (Hewett et al. 1985). Separately, grism images were obtained of the fields at Las Campanas Observatory with the 2.4 m Du Pont Telescope, and these were also scanned with the APM system. Several quasar candidates were identified from this effort, one of which was relatively bright, with $V \sim 17$, and which had a tentative redshift of $z_{\text{em}} = 2.24$. Moderate-resolution spectroscopy with the Anglo-Australian Telescope and the CTIO 4 m telescope confirmed this redshift and established that numerous absorption lines were present at wavelengths down to the atmospheric limit. Although we had hoped to identify a higher redshift quasar within the southern CVZ,

none of the other candidate objects were acceptable, so this quasar was deemed provisionally satisfactory for our purposes.

To further ascertain the suitability of the quasar for the HDF-S, it was observed at 20 cm with the Australia Telescope Compact Array (ATCA) to determine whether any unacceptably bright radio sources were located in the region that would compromise deep radio studies of the field. At the same time, a program of optical photometry of the quasar was undertaken at CTIO to determine its photometric properties, the results of which are described in the Appendix. The ATCA observations established that the quasar itself was not a strong radio source, having $S_{20\text{ cm}} < 3$ mJy, but that a relatively strong radio source was located $10'$ from the quasar ($S_{20\text{ cm}} = 146$ mJy). Despite initial concerns that the strong radio source might limit the noise levels attainable in deep radio observations of this field, and that a nearby bright star with $V = 7$ located approximately $9'$ northwest of the quasar might similarly compromise visible ground-based follow-up, the relatively bright optical magnitude of the quasar and the consequent ease with which high-resolution spectra could be obtained for it led the HDF-S team to select the quasar to define the line of sight for the HDF-S. With coordinates $\alpha = 22^{\text{h}}33^{\text{m}}37^{\text{s}}.6$, $\delta = -60^{\circ}33'29''$ (J2000.0), corresponding to Galactic coordinates $(l, b) = (328^{\circ}, -49^{\circ})$, this line of sight passes closer to the Galactic center than the HDF-N's, and therefore substantially more stars are located in the HDF-S WFPC2 field than the 10 that were identified in the HDF-N.

Various configurations of the quasar in the different instruments were considered for the HDF-S observations. It was ultimately decided that spectroscopy with STIS in the UV was highly desirable for the detection of Ly α systems over a wide range of redshifts, as was deep imaging of the region immediately surrounding the quasar with the high STIS resolution and throughput. With STIS pointed at the QSO, the positions of the WFPC2 and NICMOS fields were dictated by the orientation of the telescope at the time of the best CVZ passage through the field, by the positions of guide stars, and by the desire to avoid several bright stars in the area. The final configuration resulted in the WFPC2 and NICMOS camera 3 (NIC3) fields being undistinguished in nature. The separation between the WFPC2 and STIS field centers is 5:1, corresponding to a comoving separation of 8.3 Mpc for redshift $z = 1$ and a cosmology with $H_0 = 65$ km s $^{-1}$ Mpc $^{-1}$, $\Omega_m = 0.3$, $\Omega_\Lambda = 0.7$, and $\Omega_{\text{tot}} = 1$ (the fiducial cosmology we shall adopt throughout this paper). The separation between the NIC3 and STIS fields is 7:7, corresponding to 13 Mpc for the same cosmology. Thus, the galaxy statistics in the WFPC2 and NIC3 fields are unlikely to be much influenced by clustering around the QSO.

Figure 1 shows the *HST* instrument footprints for the primary HDF-S fields, superposed upon a CTIO 4 m image of the region obtained with the Big Throughput Camera.

3. OBSERVING PROGRAM

Commensurate with the HDF-N observing campaign, the decision was taken to devote 150 consecutive orbits to observing the HDF-S primary fields. The observing strategies for each of the three *HST* instruments were independent, inasmuch as each of them views a separate field and provides different observing capabilities. However, for the purposes of creating the observing schedule, STIS was

TABLE 1
OBSERVING MODES FOR THE HDF-S DEEP FIELDS

Filter/Grating	Total Exposure Time (s)	Number of Exposures
WFPC2 imaging:		
F300W (<i>U</i>)	140,400	106
F450W (<i>B</i>).....	103,500	67
F606W (<i>V</i>)	99,300	53
F814W (<i>I</i>)	113,900	57
NIC3 imaging:		
F110W (<i>J</i>).....	162,600	142
F160W (<i>H</i>)	171,200	150
F222M (<i>K</i>)	105,000	102
STIS imaging:		
50CCD (clear).....	155,600	67
F28X50LP	49,800	64
MIRFUV.....	52,100	25
MIRNUV	22,600	12
Spectroscopy:		
G430M	57,100	61
G140L	18,500	8
E230M.....	151,100	69
G230L	18,400	12

treated as the primary instrument, and the exposures of the other two instruments were adjusted to fit within the constraints imposed by STIS.

A summary of the observations on the primary fields of the three *HST* instruments is presented in Table 1, where the observing modes and exposure times are listed. In addition, in Figure 2 we present a graphical summary of the observations with each instrument and the modes we used, with the wavelength regions covered, the limiting magnitudes or equivalent widths achieved, and the spectral resolution. More detailed descriptions of the observations with each of the instruments and the data obtained are presented in the separate instrument-specific papers that are referenced below.

3.1. WFPC2

After consideration of various alternatives, we chose essentially the same WFPC2 program that had been adopted for the HDF-N, i.e., performing imaging with the F300W, F450W, F606W, and F814W broadband filters (where the numbers give the approximate central wavelengths in nanometers). The F300W exposures were taken during the daylight sector of the orbit, when the scattered-light background is high. The lower quantum efficiency of WFPC2 in the UV causes these exposures to be read-noise limited, so they are not significantly degraded by the higher scattered-light background. The rationale for the allocation of imaging time in the different filters was given in Williams et al. (1996).

The results of the HDF-S WFPC2 imaging campaign and the resultant source catalog are described in detail in the accompanying paper by Casertano et al. (2000).

3.2. NICMOS

In the case of the NICMOS observations, useful data were limited to the $51'' \times 51''$ field of NIC3. Cameras 1 and 2 (NIC1 and NIC2) did not gather useful scientific data, because of the loss of confocality of NIC1 and NIC2 with NIC3 that occurred as a result of thermal stresses encountered by NICMOS during the prelaunch testing period. Although NIC3 itself is not confocal with the other instru-

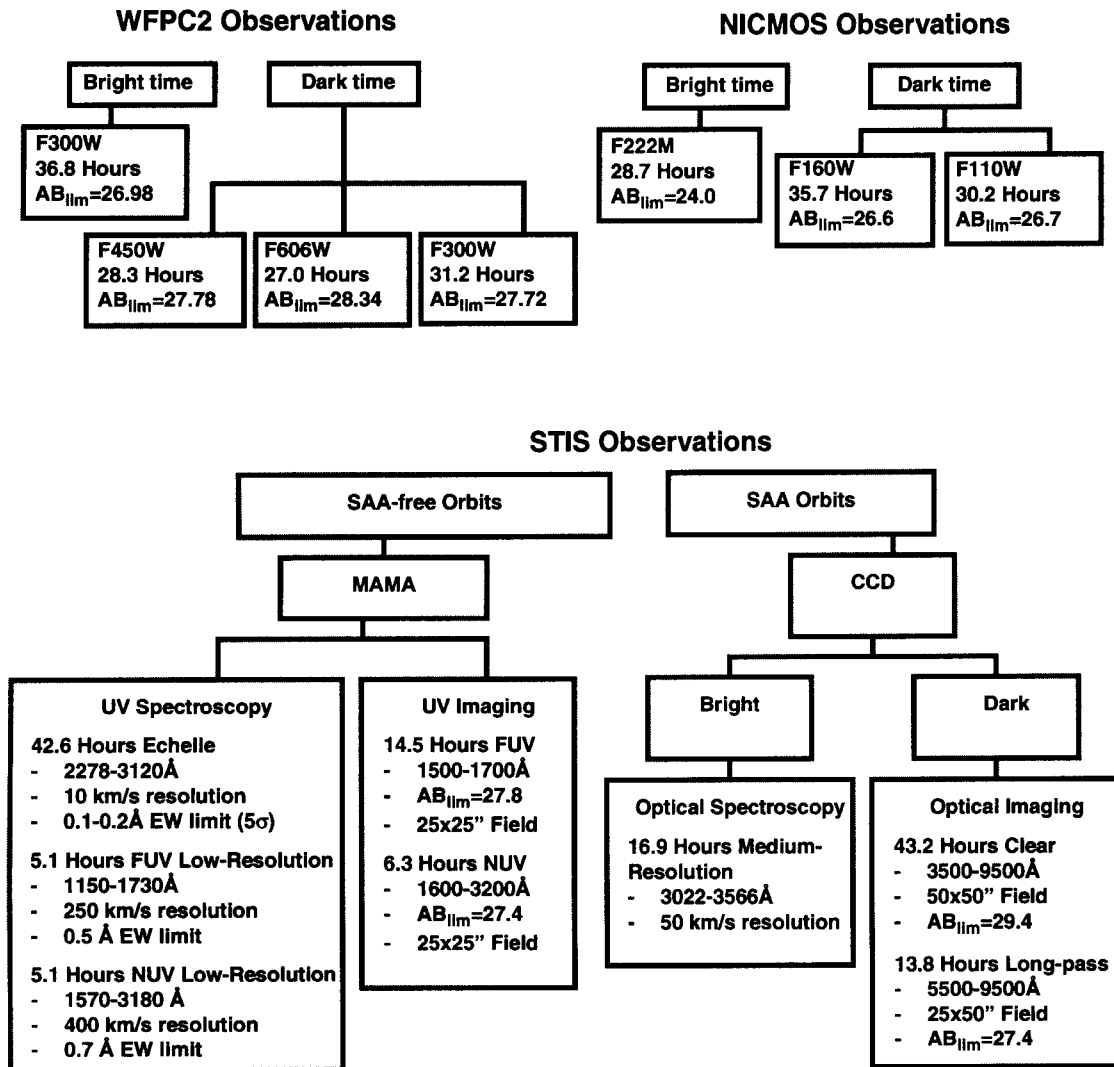


FIG. 2.—Summary of the observations made with WFPC2, STIS, and NIC3. For WFPC2 and STIS, the limiting magnitudes are 10σ values based on the rms noise in an aperture area of 0.2 arcsec^2 . For NICMOS, the magnitude limits refer to an aperture area of 0.5 arcsec^2 . For the STIS spectroscopic observations, the equivalent width limits and spectral resolutions refer to 2 detector pixels and assume spectra are extracted with equal weights in the cross-dispersion direction.

ments, the travel of the NICMOS pupil alignment mechanism did allow an independent focus to be achieved with NIC3 that was acceptable, at the expense of poor focus in the other two cameras. We chose to use NIC3 exclusively for imaging in the *J* (F110W), *H* (F160W), and *K* (F222M) bands. Obtaining slitless grism spectroscopy of the NIC3 field, while it would have been scientifically interesting, was left for future observers. To obtain high-quality spectra for all of the objects in the field would require changing the telescope roll angle more than we did during the HDF-S campaign. The high *HST* background in the *K* band due to radiation from the warm telescope causes these images to be unaffected by the increased sky background during the daylight portion of the orbit, so *K*-band images were obtained only during daylight. The dark halves of the orbits were devoted entirely to imaging in the *J* and *H* bands, apportioned roughly equally between the two filters.

An electronic artifact sometimes appears in images from NIC3 when it is read out independently of the other two cameras. To avoid this, exposures were also taken with NIC1 and NIC2, even though they were severely out of focus. The data from these cameras were not reduced

beyond standard pipeline processing but are nevertheless available in the *HST* archive.

The results of the NIC3 images and data reduction procedures, and the resultant source catalog, are described by Fruchter et al. (2000).

3.3. STIS

With its large number of imaging and spectroscopic modes, STIS presented the greatest variety of observing alternatives. Having chosen to center the STIS field on the quasar, we scheduled the majority of time for imaging of the field and for UV spectroscopy of the quasar, the latter of which could be done during the daylight half of the orbit because of the brightness of the quasar. As STIS does not have a wide selection of filters to create a multicolor data set, most of the STIS imaging was done in its 50CCD clear mode to achieve maximum depth. The 50CCD mode provides an extremely wide (2500 \AA FWHM) bandpass centered at approximately 5800 \AA . Very rough color information in the visual was obtained from additional images taken with the F28X50LP filter centered at approximately 7200 \AA , and from near- and far-UV (2360 and 1600

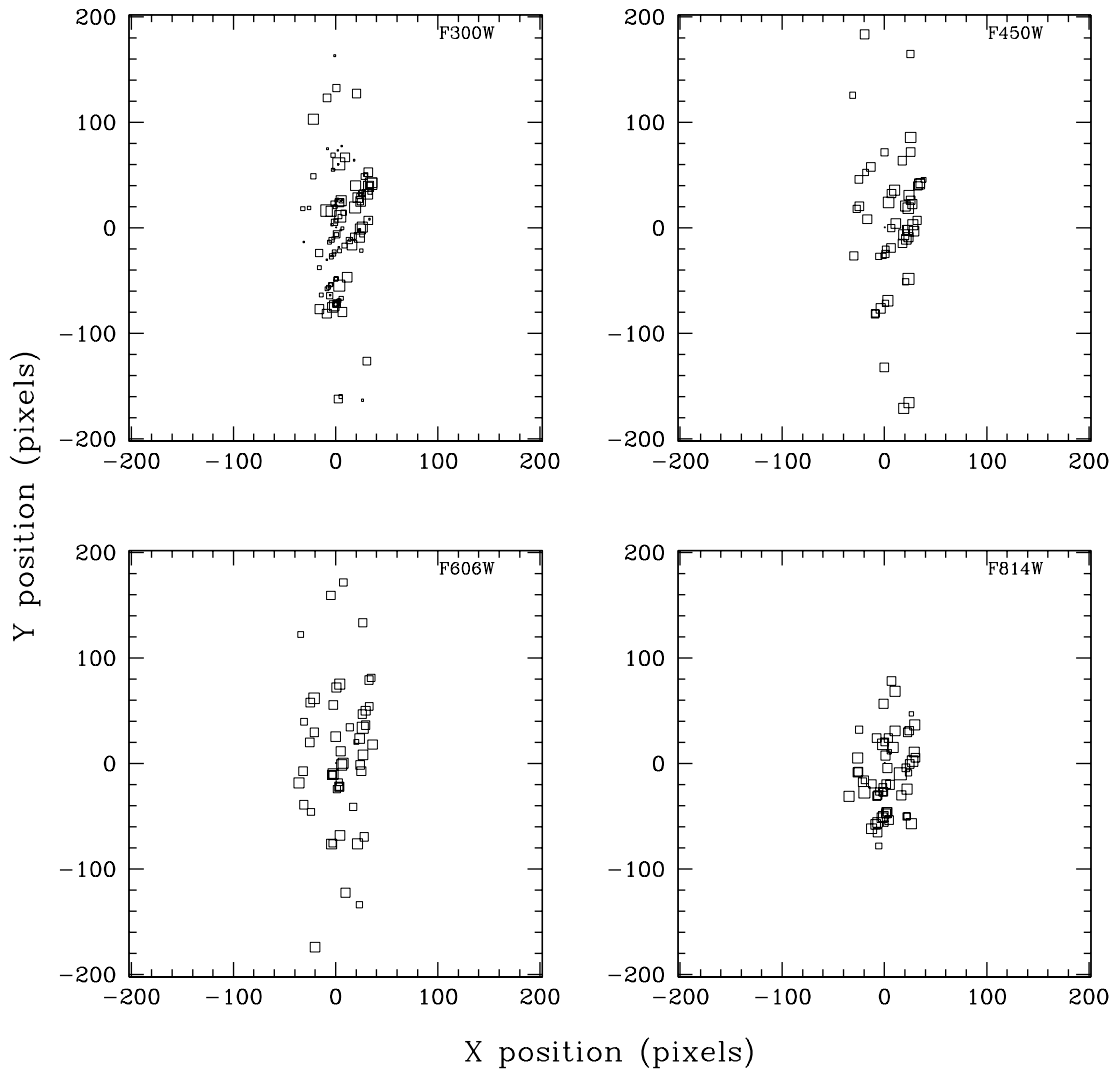


FIG. 3.—Diagram of the dither pattern as it appears on WFPC2 chip 2. The elongation in the vertical direction is a result of the fact that much of the dithering was achieved by rotating the field while keeping the QSO fixed in the STIS spectroscopic aperture. The dither positions shown here are based on planned motions rather than detailed astrometry of the individual images.

Å) images of the field obtained with the MAMA detectors. Full details of the STIS imaging observations and reductions, and the catalog of objects, have been presented by Gardner et al. (2000).

The decision regarding the selection of STIS spectroscopic modes took into account the fact that good high-resolution optical spectra of the HDF-S quasar, J2233–606, had already been acquired from the ground (Savaglio 1998; Outram et al. 1999) and, therefore, STIS could concentrate on the UV spectral region. Detection of Ly α absorption and possible associated metal lines requires a good signal-to-noise ratio (S/N) and benefits from a spectral resolution that approaches that of the intrinsic line widths. The echelle format offered by STIS in the near-UV with the MAMA detector provides for excellent resolution (10 km s^{-1}) over a wide spectral range and in a wavelength region of interest for detection of Ly α systems. In terms of detecting the maximum number of narrow lines in the minimum amount of time, the E230M mode was clearly the optimum choice.

We considered it important to obtain spectral data from the quasar over the entire wavelength regime from below rest Ly α to the $z = 2.24$ redshifted Ly α emission line at

3950 Å. A preliminary two-orbit test spectrum of the quasar obtained by *HST* in 1997 had shown the existence of a Lyman continuum absorption edge at redshift $z = 1.9$, which suppresses the quasar continuum in the 1600–2650 Å wavelength region. Emphasis was therefore placed upon using the echelle to obtain very good spectral data in the region extending in wavelength from this Lyman continuum edge up to the atmospheric cutoff, above which ground-based telescopes can take over. In addition, lower resolution spectra of the quasar were acquired over the entire region from 1150 to 3550 Å, providing for overlap of the spectra obtained with the different gratings and detectors. A full description of the STIS spectroscopy of J2233–606, including the line strengths and identifications, is presented by Ferguson et al. (2000b).

3.4. Dithering Strategy

Most *HST* observations benefit greatly from small, systematic pointing changes between exposures, or dithering. Changes of several pixels help smooth and remove pixel-scale artifacts such as flat-field features and bad pixels. Fractional pixel shifts help recover spatial information that

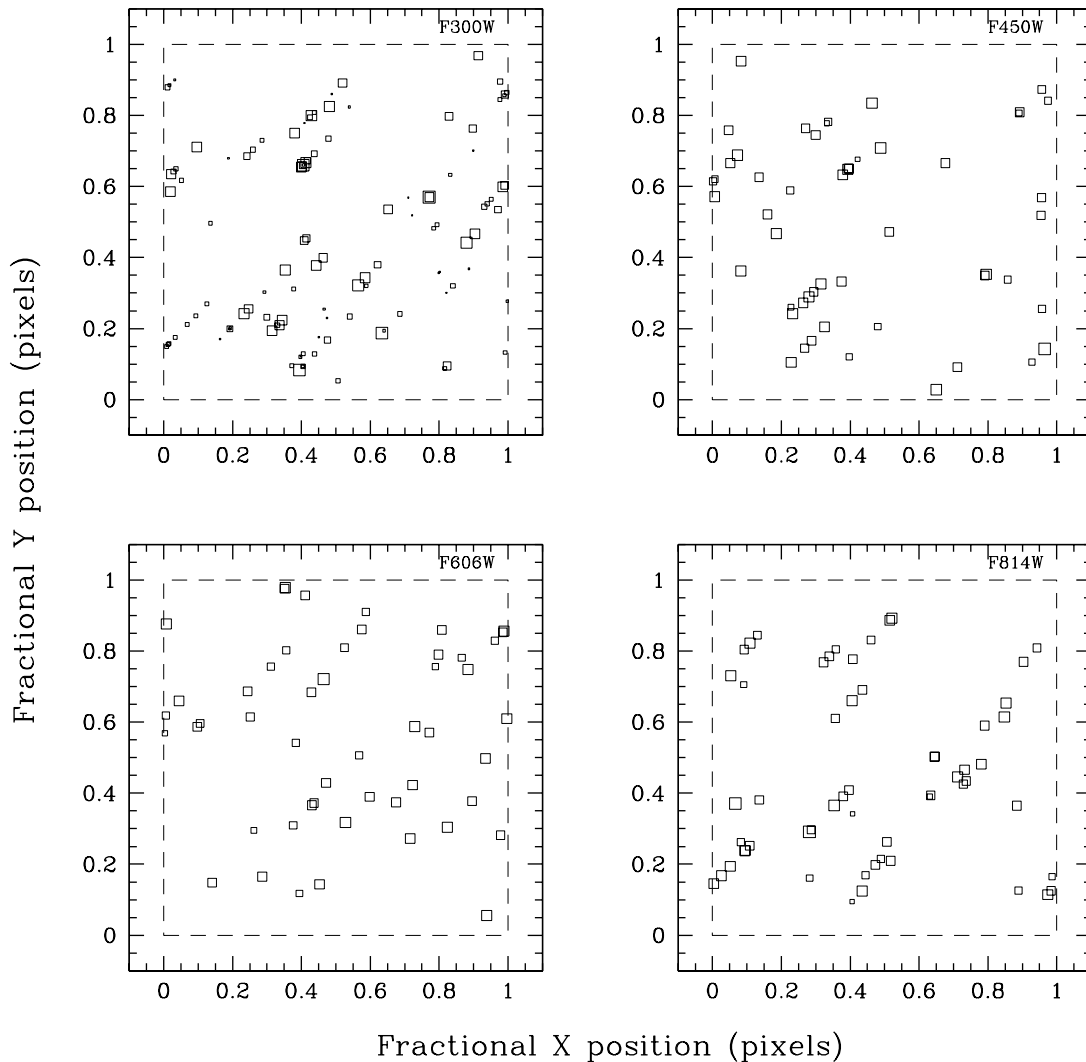


FIG. 4.—The subpixel dither pattern as it appears at the center of WFPC2 chip 2. The dither positions shown here are based on planned motions rather than detailed astrometry of the individual images.

is lost by undersampling when the pixel size exceeds the point-spread function, as it does for the Wide Field (WF) Cameras and NIC3. The original HDF-N observations used a dithering pattern that consisted of parallel displacements of the telescope of the order of $2''$ in each coordinate while keeping the telescope roll angle, i.e., the orientation of the field of view on the sky, constant. A nine-point dither pattern was employed to produce fine sampling of the point-spread function on subpixel scales.

The HDF-S observations required a different strategy because of the large amount of time spent in STIS spectroscopic modes targeted on the quasar. Spectroscopic observations impose the constraint that the target must be maintained on the slit or one of the echelle apertures, leaving no freedom to change the pointing perpendicular to the slit. That constraint can be circumvented to a large extent by rolling the telescope about the target, resulting in pointing shifts that vary with distance from the target. However, no observing strategy used in parallel with STIS spectroscopy can result in a regular dither pattern across the full field of view of the other instruments.

Because of this situation, we decided to use two distinct dithering schemes. When STIS was used in imaging mode,

we employed a nine-point square pattern with constant roll angle, i.e., pure translation, much as was done for the original HDF-N observations. The dither step was $\pm 2''.52$ in the orthogonal directions parallel to the columns and rows of the detectors, corresponding to subpixel shifts of approximately $\frac{1}{3}$ of a pixel each for the Planetary Camera (PC), WF, and NIC3 detectors (55.3 PC pixels, 25.3 WF pixels, and 12.3 NIC3 pixels). All observations made in parallel with STIS spectroscopy used a different dither pattern employing a number of shifts along the slit combined with rotations, so as to produce a quasi-random distribution of pointing shifts at both the pixel and subpixel scales. The resulting large-scale dither pattern is illustrated in Figure 3 for the WF2 detector. Although no regular pattern could be obtained, we were able to achieve a net result of near-uniform subpixel coverage everywhere in the different fields of view. We used five different roll angles: nominal roll, for which the Y-axis of the STIS CCD was roughly 5° west of north, and four additional orientations at $\pm 0.6^\circ$ and $\pm 1.0^\circ$ from the nominal roll angle. These roll angles were chosen to produce a good subpixel pattern in the center of each of the WFPC2 detectors and the NIC3 detector. Changes in roll angle were also employed with the five different sub-



FIG. 5.—Mosaic of the HDF-S primary and flanking fields. All fields from WFPC2, STIS, and NICMOS are included.

apertures used in the echelle mode, and $\pm 2''.52$ shifts along the slit were made in long-slit mode, to obtain a total of 35 different subpointings for all observations made in parallel with STIS spectroscopy. An example of the resulting subpixel dither pattern is shown in Figure 4 for the WF2 detector.

Whenever possible, we attempted to maintain the same combination of roll angle and subaperture/shift for consecutive exposures using the same filters. This resulted in a number of same-pointing, same-filter exposure pairs that could be used for direct cosmic-ray rejection. These pairs were the starting point for the first-pass pointing determination described in the paper devoted to the WFPC2 imaging (Casertano et al. 2000).

3.5. Flanking Fields

As with the HDF-N, a modest amount of time, 27 orbits, was devoted to WFPC2 imaging of flanking fields adjacent to the primary fields in order to provide for morphological and photometric information for objects studied in ground-based follow-up in the vicinity of the three primary fields. A mosaic of contiguous WFPC2 images in the *I* band of two orbits each were taken in the area of sky between the primary WFPC2 and STIS fields, and extending down to

cover the NIC3 field. The exposures for each flanking field consisted of four dither positions, and each of the WFPC2 flanking fields also has an STIS (50CCD) and a NIC3 (*H* band) field associated with it. These latter fields are not contiguous, because the field sizes of both STIS and NIC3 are smaller than that of WFPC2.

In addition, as part of the flanking fields program we imaged the primary NIC3 field with STIS for nine orbits in the 50CCD clear mode, thereby providing a short-wavelength baseline for color information of that field. The complete mosaic of flanking fields is shown in Figure 5, and the observations and data reduction will be described more fully by Lucas et al. (2000).

4. DATA REDUCTION

The data reduction procedures are set out in detail in each of the associated papers. Nevertheless, it is worth introducing here the procedures used for image combination and image defect rejection because they were similar for the WFPC2, NIC3, and STIS CCD imaging. The dithering strategy adopted for the HDF-S made it impossible to remove cosmic rays by stacking images taken at identical pointings, because in many cases there were only a few images taken at a common position. Instead, the

cosmic-ray rejection involved several steps of geometric transformation and filtering.

A first cut at image registration was made using one of several methods. Where available, pointing information from the Fine Guidance Sensors, as recorded in the jitter file, was used to derive positions relative to a standard reference image. In many cases this was checked either using cross-correlation or the positions of individual sources. The images were shifted and rotated to the same frame using the variable-pixel linear reconstruction algorithm of Fruchter & Hook (1998). This algorithm, also referred to as “drizzling,” was used for the HDF-N observations, and it corrects for geometric distortions and allows different pixel sampling of the input and output images. It also allows individual pixels to be weighted optimally and propagates these weights appropriately during the image combination.

In the first pass, the images were drizzled into the same reference frame and a median image was constructed. This median image was then transformed back to the reference frame of each individual image and was used as a reference for rejection of cosmic rays or other defects. The image registration was then refined by cross-correlating the cosmic-ray-masked image against the median image. Static detector flaws, e.g., hot pixels or bad columns, were also masked in this step. Finally, the cosmic-ray-masked images were combined using weights derived from a noise model, where the weights were chosen to optimize the S/N at the level of the mean background.

The choice of output sampling varied from instrument to instrument. For the deep images, the output pixel scale was roughly half the input pixel scale. Improvement in resolution was obtained by adjusting the PIXFRAC parameter in the DRIZZLE task so that the pixels from each image were added into the final image with a smaller footprint (see Williams et al. 1996 for a more complete discussion). A common feature of the final images is that the noise is correlated between adjacent pixels, so the S/N of the images should not be determined by measuring rms fluctuations on a scale of individual pixels.

5. THE CATALOGS

Detection and photometry of faint galaxies constitute a difficult problem. The ideal goal is to detect all sources down to a fixed isophotal threshold. In practice, the varying S/N across an image, the varying sizes and shapes of galaxies, and the frequent superposition of different objects make it extremely difficult to achieve this goal. Different photometry codes make different compromises to approach this ideal, and the extent to which these compromises matter depends on the scientific investigation being pursued. Measurements of small-scale clustering or searches for the galaxies responsible for QSO absorption lines, for example, may be strongly affected by the merging or splitting of objects with overlapping isophotes. On the other hand, for counting galaxies the merging and splitting details are a second-order effect (Ferguson 1998). Searches for Lyman break galaxies are sensitive to how the flux is distributed between overlapping objects when doing the photometry, even if the two objects are correctly cataloged as separate entities.

The HDF-S catalogs have been produced using the SExtractor package (Bertin & Arnouts 1996). The HDF-N catalog of Williams et al. (1996) was constructed using FOCAS (Tyson & Jarvis 1979). To allow direct comparison

of the two data sets, we have created a new catalog of the HDF-N data set using SExtractor with the same parameters used for the HDF-S. A major motivation for using SExtractor was the ability to use weight and rms maps to modulate the detection threshold and to compute the final photometric errors for each source.

While SExtractor does a reasonable job of detecting faint objects in the wings of bright ones, no single set of deblending thresholds, cleaning parameters, etc., was deemed acceptable for the definition of sources over the wide range of conditions encountered in the set of HDF-S images. In particular, the set of parameters that did the best job for detecting the typical faint, relatively isolated galaxies would tend to overmerge galaxies near bright stars, counting them as part of the star rather than keeping them as separate objects. While this has a negligible effect on faint-galaxy statistics, it would produce a catalog that did not have separate entries for a number of objects that might be good candidates for spectroscopy. To recover these objects, SExtractor was run multiple times with different detection thresholds. Objects that were considered to be “overmerged” in the first catalog were deleted from that catalog, and the entries for their various subcomponents were taken from a catalog with a higher detection threshold. A few obvious artifacts due to diffraction spikes were deleted from each catalog as well. The object numbering and the flags indicate whether the parameters for the source came from the first or subsequent runs of SExtractor. The number of objects added to and deleted from the different catalogs from application of different threshold parameters were as follows: WFPC2, 25 deleted, 32 added; STIS, 26 deleted, 8 added; and NICMOS, 14 deleted, 29 added.

The SExtractor catalogs contain more than 100 parameters that characterize each object, including positions, photometry in different apertures, and measures of size, ellipticity, and position angles. The versions of the catalogs in the instrument-specific papers contain just the basic photometric information. Electronic versions of the entire catalogs, including the SExtractor catalog for the HDF-N, can be obtained from the HDF-S World Wide Web site.¹⁴

6. ASTROMETRIC COORDINATE SYSTEM

In order to facilitate the further study of the HDF-S, especially at other wavelengths, an accurate coordinate system has been established for the HDF-S fields, linking them to the *Hipparcos* coordinate system and thus the International Celestial Reference System (ICRS). A three-step procedure was employed to tie the fainter stars in the HDF-S region to the brighter reference standards situated outside of the immediate fields, similar to that used for the USNO-Hamburg radio-optical reference frame project (Zacharias et al. 1995). A description of the procedure and first results of the astrometry have been presented elsewhere (Zacharias et al. 1998).

First, between 1998 July and September the USNO CCD Astrograph (UCA) was used to take 42 frames of the HDF-S region, covering a 1.2-wide square field. The UCA is currently located at CTIO in order to carry out the Southern Hemisphere observations that will be used for the UCA Catalog (Zacharias 1997). It consists of a 206 mm aperture, five-lens 2 m focal length astrometric instrument

¹⁴ At <http://www.stsci.edu/ftp/science/hdfsouth>.

with a Kodak 4K × 4K CCD camera. The CCD frames were reduced directly to the *Hipparcos* system, primarily using the US Naval Observatory ACT Reference Catalog (Urban, Corbin, & Wycoff 1998), to provide positions for secondary reference stars in the $R = 10\text{--}16$ mag range (5790–6420 Å bandpass). A total of 1085 astrometrically suitable stars were selected, with individual positional precisions of 5–40 mas per coordinate and with a zero-point error estimated to be approximately 20 mas.

Second, six frames of the entire region were obtained in 1998 September with the Cerro Tololo 0.9 m telescope plus standard 2K CCD camera using a dedicated filter to match the bandpass of the astrograph observations. Two overlapping 0.9 m fields were used to cover all of the HDF-S fields, and the images were reduced using 73 to 82 secondary reference stars for each CCD frame from the previous astrograph observations. The errors of the least-squares adjustments were found to be 23–28 mas using a linear model after correction for optical distortions, and the zero-point error with respect to the system of the secondary reference stars was estimated to be about 5 mas.

The third step in the process consisted of selecting 279 astrometrically suitable tertiary reference stars from the 0.9 m data, to be used for the reductions of the *HST* images themselves. These stars are in the magnitude range $R = 12\text{--}21$, and they cover an area of $12' \times 18'$ with precisions of 5–20 mas. Between two and 10, with an average of four, stars from the 0.9 m data were used for the reduction of individual WFPC2 fields, using offset-only linear models giving an rms error of 25 mas. For the STIS CCD flanking fields, insufficient stars from the 0.9 m were available, so CTIO 4 m Big Throughput Camera images were used as an intermediate step with an estimate of the position error of under 100 mas. On the basis of the CTIO 0.9 m data, the ICRS coordinates of the HDF-S quasar, J2233–606, are determined to be $\alpha = 22^{\text{h}}33^{\text{m}}37^{\text{s}}.5883$, $\delta = -60^{\circ}33'29''.128$. The total systematic error in the *HST* positions from the combination of all steps is estimated to be approximately 30 mas.

7. CONCLUSIONS

This paper serves as an introduction to the series of instrument-specific papers on the HDF-S, which outline the motivation for the observations, the observing strategy, and the schematic steps used in reducing the data and cataloging the sources. The companion papers (Casertano et al. 2000; Ferguson et al. 2000b; Fruchter et al. 2000; Gardner et al. 2000; Lucas et al. 2000) provide the full technical details of the observations and data reduction, and some basic statistical results from the samples. Detailed analysis of the HDF-S field is well underway (e.g., Savaglio et al. 1999; Benítez et al. 1999; Abraham et al. 1999; Madau & Pozzetti 2000) and will undoubtedly increase as major new instruments come on line in southern ground-based observatories.

It is a pleasure to thank the US Naval Observatory CCD Astrograph team and CTIO for making possible the astrometric link of the HDF-S positions to the ICRS. We are grateful as well to our many colleagues who shared their ground-based data with us in advance of publication, thus allowing us to optimize our observing strategies. This work

was supported by grants GO-07633.01-96A and GO-8058.01-96A and Hubble Fellowships HF-01083.01-96A (C. L. M.) and HF-1079.01-96A (C. M. C.) from the Space Telescope Science Institute, which is operated by the Association of Universities for Research in Astronomy, Inc., under NASA contract NAS 5-26555. The APM, used to identify the quasar, is a national astronomy facility run by the Cambridge Astronomical Survey Unit at the Institute of Astronomy, Cambridge.

APPENDIX

PHOTOMETRY OF QSO J2233–606

Following the selection of the field for the HDF-S, we began a program to photometrically monitor the quasar to establish its properties and to look for obvious variability that might impact the planned *HST* observations with STIS, which requires protection from bright objects. CCD imaging of the field surrounding the quasar was made with the CTIO 0.9 m telescope using the facility CCD camera on the five nights of 1997 July 6, 14, and 23, 1997 December 8, and 1998 October 2 (UT). Only two of the nights (July 14 and October 2) were photometric, and the same techniques and $UBV(RI)_{\text{KC}}$ facility filters employed by Suntzeff et al. (1999) were used to establish local standards around the quasar. On 1997 July 14, 22 independent standards were observed with seven separate telescope pointings over an air-mass range of 1.1–1.7. On 1998 October 2, we observed 28 independent standards in 15 telescope pointings over an air-mass range of 1.1–1.5. On both occasions the HDF-S field was observed at an air mass of 1.2, and the standards were taken from the lists of Graham (1982) and Landolt (1992).

For the two photometric nights, the transformation equations from the instrumental to the Johnson/Kron-Cousins systems were very similar, and therefore we used the averaged color terms in our reductions. The averaged color terms for the two nights differ by less than 0.01 mag per mag when compared with the color terms adopted by Suntzeff et al. (1999). We have selected 14 isolated stars in the field surrounding the quasar to use as local standards, and these stars are identified in Figure 6. Comparing the BV photometry of the 14 local standards on the two photometric nights, we find the mean difference, the median difference, and the dispersion in the differences to be 0.014, 0.013, and 0.009 for V and 0.000, 0.006, and 0.029 for $B-V$, respectively. The mean errors are the dispersions divided by $14^{1/2}$.

In addition, the brightnesses of all the stars in the quasar field were determined for all five nights of observations with point-spread function (PSF) techniques using Stetson's DAOPHOT programs (Stetson 1987) and transformed to standard colors using the 14 local standards and the averaged color terms. The average results of this combined photometry of the local standards over the five nights are presented in Table 2. The last four columns of the table give the number of independent frames that went into the averages. The statistical mean errors are also listed in the table in units of 0.001 mag. The final error in the measured brightness is obtained by adding to these values, in quadrature, the error in the overall photometric zero point. From

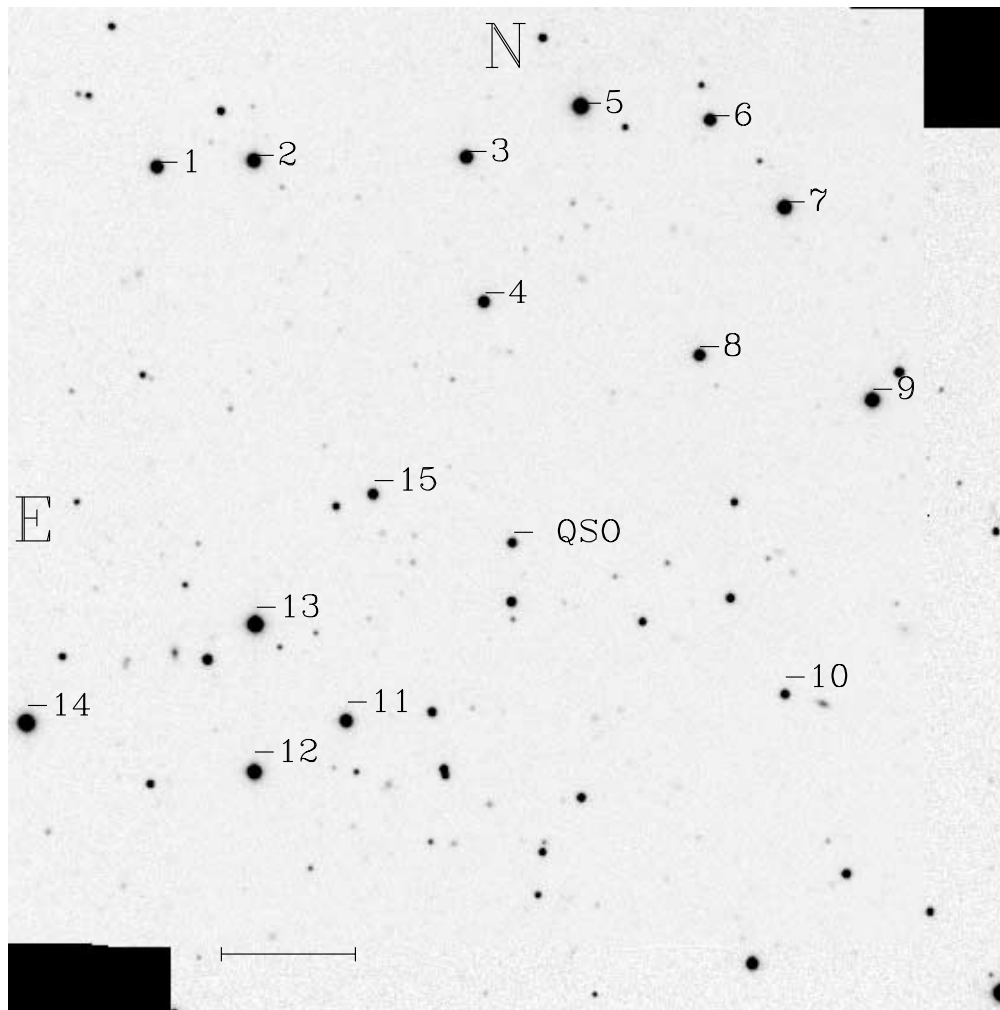


FIG. 6.—Finding chart for the local photometric standards in the vicinity of the HDF-S quasar. This composite image was made from all the HDF-S frames taken in B and V with the CTIO 0.9 m telescope in 1997. A scale bar of length $1'$ is shown in the lower part of the image.

the numbers quoted in the previous paragraph, this is roughly 0.01 mag in B and V , based on the two nights of photometric observations.

The results of the PSF photometry of the quasar are

presented in Table 3. It is evident that over the year of the observations, which includes the time of the *HST* HDF-S observing campaign, the brightness of the quasar was quite constant at $V = 17.15$.

TABLE 2
 $BVRI$ PHOTOMETRY OF LOCAL STANDARDS NEAR THE HDF-S QUASAR

No.	V	$B-V$	$V-R$	$V-I$	n_B	n_V	n_R	n_I
1	15.515 (004)	0.597 (006)	0.375 (006)	0.760 (011)	5	5	1	1
2	14.856 (003)	0.799 (004)	0.462 (006)	0.886 (010)	6	6	1	1
3	15.369 (004)	0.499 (006)	0.311 (010)	0.660 (025)	6	6	1	1
4	15.751 (003)	0.883 (005)	0.462 (014)	0.937 (022)	6	6	1	1
5	14.142 (003)	0.861 (005)	...	0.913 (012)	5	5	0	1
6	15.819 (004)	0.669 (006)	0.398 (021)	0.780 (028)	5	5	1	1
7	14.856 (003)	0.616 (005)	0.377 (012)	0.752 (015)	6	6	1	1
8	15.890 (003)	0.655 (005)	0.362 (028)	0.752 (022)	6	6	1	1
9	14.389 (007)	1.382 (011)	4	4	0	0
10	17.236 (004)	0.508 (006)	0.339 (008)	0.714 (012)	6	6	1	1
11	15.180 (005)	0.969 (007)	0.566 (009)	1.087 (012)	6	6	1	1
12	14.492 (003)	1.020 (005)	0.557 (005)	1.069 (010)	6	6	1	1
13	14.013 (003)	0.855 (004)	...	0.914 (010)	6	6	0	1
14	14.032 (005)	0.682 (007)	...	0.747 (011)	4	4	0	1
15	16.131 (003)	1.350 (008)	0.851 (006)	1.634 (010)	6	6	1	1

TABLE 3
PHOTOMETRY OF THE HDF-S QUASAR

Date (UT)	JD (2,450,000+)	V	$B-V$	$V-R$	$V-I$	n_B	n_V	n_R	n_I
1997 Jul 14.....	643.9	17.127 (006)	0.164 (010)	2	2	0	0
1997 Jul 23.....	652.8	17.138 (012)	0.162 (019)	1	1	0	0
1997 Dec 8.....	790.5	17.171 (013)	0.160 (023)	1	1	0	0
1998 Sep 3.....	1,059.7	17.142 (007)	0.153 (022)	2	2	0	0
1998 Oct 2.....	1,088.5	17.150 (009)	0.176 (016)	0.280 (013)	0.642 (016)	1	1	1	1

REFERENCES

- Abraham, R. G., Merrifield, M. R., Ellis, R. S., Tanvir, N. R., & Brinchmann, J. 1999, *MNRAS*, 308, 569
Aussel, H., Cesarsky, C. J., Elbaz, D., & Starck, J. L. 1999, *A&A*, 342, 313
Benítez, N., Broadhurst, T., Bouwens, R., Silk, J., & Rosati, P. 1999, *ApJ*, 515, L65
Bertin, E., & Arnouts, S. 1996, *A&AS*, 117, 393
Casertano, S., et al. 2000, *AJ*, 120, 2747
Cohen, J. G., Cowie, L. L., Hogg, D. W., Songaila, A., Blandford, R., Hu, E. M., & Shopbell, P. 1996, *ApJ*, 471, L5
Connolly, A. J., Szalay, A. S., Dickinson, M., SubbaRao, M. U., & Brunner, R. J. 1997, *ApJ*, 486, L11
Désert, F.-X., Puget, J.-L., Clements, D. L., Pérault, M., Abergel, A., Bernard, J.-P., & Cesarsky, C. J. 1999, *A&A*, 342, 363
Dickinson, M. 1998, in *The Hubble Deep Field*, ed. M. Livio, S. M. Fall, & P. Madau (Cambridge: Cambridge Univ. Press), 219
Dickinson, M., et al. 2000, *ApJ*, 531, 624
Ferguson, H. C. 1998, in *The Hubble Deep Field*, ed. M. Livio, S. M. Fall, & P. Madau (Cambridge: Cambridge Univ. Press), 181
Ferguson, H. C., et al. 2000a, in preparation
———. 2000b, in preparation
Fomalont, E. B., Kellermann, K. I., Richards, E. A., Windhorst, R. A., & Partridge, R. B. 1997, *ApJ*, 475, L5
Fruchter, A., et al. 2000, in preparation
Fruchter, A. S., & Hook, R. N. 1998, preprint (astro-ph/9808087)
Gardner, J. P., et al. 2000, *AJ*, 119, 486
Gilliland, R. L., Nugent, P. E., & Phillips, M. M. 1999, *ApJ*, 521, 30
Graham, J. A. 1982, *PASP*, 94, 244
Gwyn, S. D. J., & Hartwick, F. D. A. 1996, *ApJ*, 468, L77
Hewett, P. C., Irwin, M. J., Bunclark, P., Bridgeland, M. T., Kibblewhite, E. J., He, X. T., & Smith, M. G. 1985, *MNRAS*, 213, 971
Hogg, D. W., et al. 1998, *AJ*, 115, 1418
Hogg, D. W., Neugebauer, G., Armus, L., Matthews, K., Pahre, M. A., Soifer, B. T., & Weinberger, A. J. 1997, *AJ*, 113, 474
Hughes, D. H., et al. 1998, *Nature*, 394, 241
Landolt, A. U. 1992, *AJ*, 104, 340
Lanzetta, K. M., Yahil, A., & Fernández-Soto, A. 1996, *Nature*, 381, 759
Lowenthal, J. D., et al. 1997, *ApJ*, 481, 673
Lucas, R., et al. 2000, in preparation
Madau, P., Ferguson, H. C., Dickinson, M. E., Giavalisco, M., Steidel, C. C., & Fruchter, A. 1996, *MNRAS*, 283, 1388
Madau, P., & Pozzetti, L. 2000, *MNRAS*, 312, L9
Mobasher, B., Rowan-Robinson, M., Georgakakis, A., & Eaton, N. 1996, *MNRAS*, 282, L7
Muxlow, T. W. B., Wilkinson, P. N., Richards, A. M. S., Kellermann, K. I., Richards, E. A., & Garrett, M. A. 1999, *NewA Rev.*, 43, 623
Outram, P. J., Boyle, B. J., Carswell, R. F., Hewett, P. C., & Williams, R. E. 1999, *MNRAS*, 305, 685
Richards, E. A., Kellermann, K. I., Fomalont, E. B., Windhorst, R. A., & Partridge, R. B. 1998, *AJ*, 116, 1039
Rowan-Robinson, M., et al. 1997, *MNRAS*, 289, 490
Savaglio, S. 1998, *AJ*, 116, 1055
Savaglio, S., et al. 1999, *ApJ*, 515, L5
Sawicki, M. J., Lin, H., & Yee, H. K. C. 1997, *AJ*, 113, 1
Steidel, C. C., Giavalisco, M., Pettini, M., Dickinson, M., & Adelberger, K. L. 1996, *ApJ*, 462, L17
Stetson, P. B. 1987, *PASP*, 99, 191
Suntzeff, N. B., et al. 1999, *AJ*, 117, 1175
Thompson, R. I., Storrie-Lombardi, L. J., Weymann, R. J., Rieke, M. J., Schneider, G., Stobie, E., & Lytle, D. 1999, *AJ*, 117, 17
Tyson, J. A., & Jarvis, J. F. 1979, *ApJ*, 230, L153
Urban, S. E., Corbin, T. E., & Wycoff, G. L. 1998, *AJ*, 115, 2161
Williams, R. E., et al. 1996, *AJ*, 112, 1335
Wilner, D., & Wright, M. C. H. 1997, *ApJ*, 488, L67
Zacharias, N. 1997, *AJ*, 113, 1925
Zacharias, N., Corbin, T., Zacharias, M., Rafferty, T. J., Seidelmann, P. K., & Gauss, F. S. 1998, *BAAS*, 30, 1367
Zacharias, N., de Vegt, C., Winter, L., & Johnston, K. J. 1995, *AJ*, 110, 3093